ICCFD13 MILAN ITALY 2026

ICCFD13-2026-263

Experimental Validation of HTLES for Shock-Induced Boundary-Layer Separation in Confined Transonic Flows

B. Geiben*,**, M. Havermann*, E. Hale** and C. Bil**
Corresponding author: geiben@fh-aachen.de
* FH Aachen, Germany
** RMIT University, Australia

Abstract:
Shock-induced boundary-layer separation in confined transonic flows is an important source of unsteady aerodynamic loading in emerging high-speed transport concepts, including evacuated tube train (ETT) configurations. Reliable and efficient prediction of the associated shock motion and buffet frequencies is therefore essential for assessing aerodynamic behaviour, structural excitation, and passenger comfort. RANS and URANS methods often predict integrated quantities, such as drag, reasonably well, yet they often cannot recover the spectral content of the shock motion and the associated unsteady loads. Hybrid Temporal Large Eddy Simulation (HTLES) has been shown to capture these unsteady shock dynamics at feasible cost. However, experimental validation is needed to confirm whether simulated shock-motion spectra are reproduced in physical measurements. This paper addresses that gap with a first experimental validation step, comparing HTLES predictions against high-speed differential-interferometry and wall static-pressure measurements of a matched transonic wind-tunnel configuration. Although a transonic indraft wind tunnel cannot reproduce all boundary and operating conditions of an ETT system, it can reproduce the key shock-wave/boundary-layer interaction (SWBLI) mechanisms needed for validation, including choking, lambda-shock formation, shock-induced separation, and global shock motion. Experimental quasi-schlieren images are compared with numerical schlieren fields from HTLES, with emphasis on shock structure, separated-flow signature, and shock-buffet spectral behaviour. The findings support HTLES as a practical tool for analysing unsteady SWBLI in confined transonic transport applications, enabling important spectral effects to be considered early in applied research and development.

Keywords: Shock-Wave/Boundary-Layer Interaction, Transonic Flow, Hybrid RANS–LES, Experimental Validation, Wind Tunnel.

1. Introduction

Blunt-body configurations are becoming increasingly relevant in transonic transport systems, yet established RANS methods often fail to reliably capture the unsteady shock dynamics that characterise this flow regime. While RANS and URANS can predict integrated quantities, such as total aerodynamic drag, with reasonable accuracy, they cannot always recover the spectral behaviour of shock-induced separation or the resulting unsteady loads that drive structural excitation and passenger discomfort [1, 2, 3]. Previous work by the authors demonstrated that Hybrid Temporal Large Eddy Simulation (HTLES), developed by Duffal, de Laage de Meux, and Manceau [4, 5], can recover these unsteady shock dynamics, which URANS did not reliably capture, while remaining computationally cost-effective [3]. However, those results lacked experimental validation. This paper addresses that gap through wind-tunnel measurements, providing a first step towards experimental validation of HTLES for confined transonic shock-wave/boundary-layer interaction (SWBLI) flows.

The flow configuration considered in the previous numerical study was motivated by evacuated tube train (ETT) concepts, generally referred to as Hyperloop, where reduced ambient pressure is utilised to reduce aerodynamic drag and thereby lower peak power and overall energy demand [6, 7]. Around the train capsule, often called the pod, the available cross-sectional area of the tube is strongly reduced. This area reduction causes substantial local flow acceleration and leads to choking once the local Mach number reaches one [7, 8, 9]. The degree of confinement is quantified by the blockage ratio BR,

$$BR = \frac{A_{\mathrm{pod}}}{A_{\mathrm{tube}}}, \tag{1}$$

where A_{pod} is the cross-sectional area of the pod and A_{tube} is the cross-sectional area of the tube. Together with the pod Mach number M_∞, the blockage ratio defines the operating regime, including whether the system remains below the isentropic choking limit, exceeds this limit, or moves towards the Kantrowitz limit, Fig. 1 [7, 10, 11]. For a given system, the blockage ratio typically remains constant, with the Mach

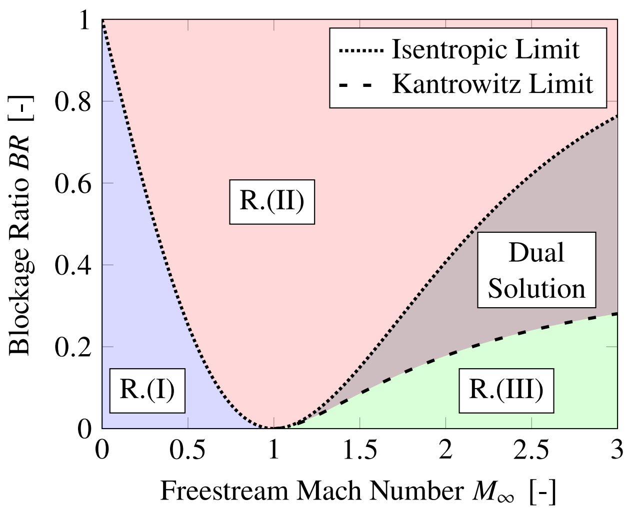

Figure 1: Isentropic and Kantrowitz limits dividing the flow-configuration space into sub-isentropic (I), super-isentropic (II), dual-solution, and super-Kantrowitz-limit (III) regimes [3].

number acting as the independent variable. Once the isentropic limit is surpassed by increasing this Mach number, shock waves form in the throat of the system [8, 9]. Within Regime (II), as shown in Fig. 1, the subsequent flow development can be divided into three categories:

(A) A temporally unstable near-normal shock, hereafter referred to as intermittent, that appears at the aft end of the pod geometry, travels upstream, breaks down, and then discontinuously reappears near the aft end, as shown in Fig. 2a.

(B) A λ-shock that may still show shock-buffet-like motion, continuously oscillating upstream and downstream around a mean position [1, 2, 3], as shown in Fig. 2b.

(C) An oblique recompression shock, including wall reflections, that forms a more extended shock system and eventually develops into a fully established shock train. These later regimes are generally more stable and show weaker large-scale shock motion [12, 13], as shown in Fig. 2c.

This study focuses on flow conditions in categories (A) and (B), where unsteady shock motion dominates the flow field near the pod and was shown in the authors' previous paper to be the most critical regime regarding reliable CFD prediction of spectral content. Although the range of operating conditions associated with buffet-like shock motion may be relatively narrow and quickly surpassed, an ETT pod operating at competitive[1] speeds in a tube of practical diameter must cross the isentropic limit during both acceleration and deceleration [7, 11]. During each passage through this regime, the pod may be exposed to spectral excitation driven by shock oscillations and shock-induced separation [1, 2]. Such unsteady loading is relevant not only for aerodynamic performance, but also for structural excitation, fatigue, and passenger comfort, and must therefore already be considered during early research and development.

[1]Competitive with commercial air travel.

(a) Cat. (A): intermittent near-normal shock motion.

(b) Cat. (B): oscillating λ-shock.

(c) Cat. (C): extended recompression shock system.

Figure 2: Shock-system development within Regime (II), illustrated by experimental quasi-schlieren images of the present configuration at increasing diffuser openings, showing the transition from intermittent near-normal shock motion to an oscillating λ-shock and, finally, to an extended recompression-shock system.

Most ETT aerodynamic studies use RANS-based CFD or lower-order models to map operating limits and integrated trends, rather than resolving shock-motion spectra [6, 7, 8]. For the near-isentropic-limit regime, however, previous HTLES results indicate that the dominant physics is closer to transonic SWBLI and shock buffet than to steady choking alone. Consistent with wave-propagation models [14] and global-mode interpretations [15, 16] of transonic shock buffet, this unsteadiness can be viewed as a coupled shock–separation process in which shock-induced boundary-layer separation (SIBLS), separated-flow dynamics, and upstream-propagating pressure or acoustic disturbances may help sustain cyclic shock motion [2]. Scale-resolving methods are therefore relevant not only for resolving turbulence, but also for capturing the separation-driven feedback mechanisms that govern buffet-like spectral behaviour. While such methods have been applied to canonical shock-separated and buffet flows with different geometries and boundary conditions [17, 18, 19], ETT-focused scale-resolving studies have mainly addressed broader choked-flow, aerothermal, or high-Mach-number regimes rather than the near-isentropic-limit regime considered here [13, 20, 21, 22]. The previous HTLES study by the authors addressed this gap numerically by showing that hybrid RANS–LES in the form of HTLES can capture the relevant buffet-like behaviour at feasible computational cost, whereas URANS did not reliably resolve these unsteady shock dynamics [3].

The present paper validates these numerical findings against in-house wind-tunnel measurements as a first step towards establishing HTLES for confined transonic SWBLI flows. The experiment is not intended to reproduce a full ETT operating environment, but to isolate the relevant physical working mechanisms in a controlled confined transonic configuration [23, 24]. The validation therefore focuses on the quantities that determine whether the unsteady SWBLI is captured correctly, such as the shock topology, the pressure-derived pre-shock Mach number, and the spectral content of the shock motion [1, 2]. By comparing these measurements with HTLES predictions, the study assesses whether HTLES provides a reliable hybrid scale-resolving alternative to URANS for early-stage analysis of confined transonic transport flows.

2. Methodology

The methodology is built around a common validation case in which the same transonic wind-tunnel configuration, Fig. 3, is investigated experimentally and numerically. The case is designed to reproduce the relevant SWBLI mechanisms of a typical aft pod geometry under near-isentropic-limit conditions. Although our experimental wind-tunnel setup cannot fully reproduce the operating and boundary conditions of a pod moving through a tube, it *does* capture the key mechanism of interest, i.e. SIBLS driving global unsteady shock motion under confined, non-freestream conditions. In this section, we first define

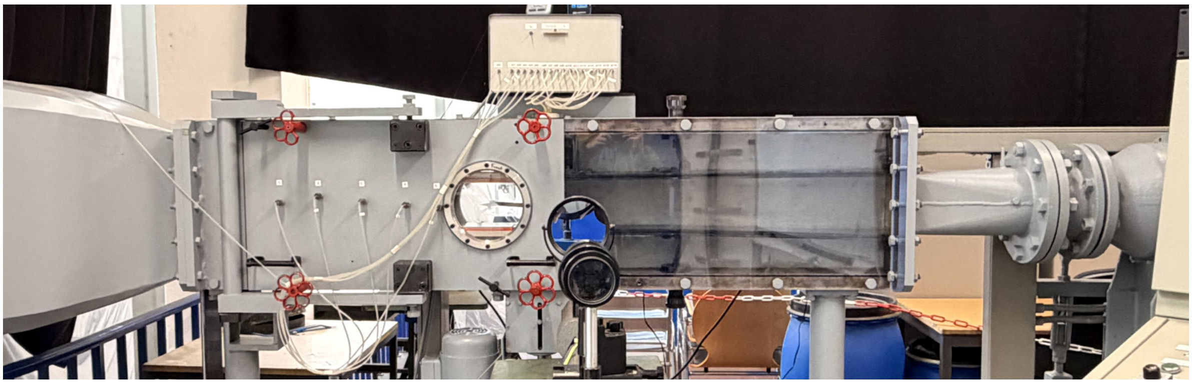

(a) Overview of the FH Aachen transonic and supersonic indraft wind-tunnel facility with door closed and diffuser fully open, including the windowed test section used for the differential-interferometry measurements.

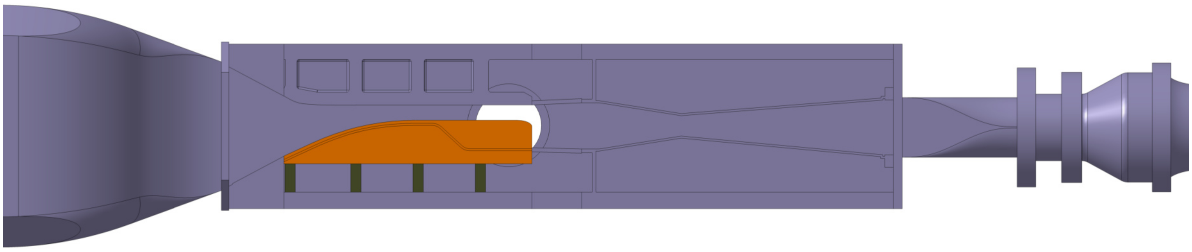

(b) CAD representation of the validation geometry, showing the interchangeable lower nozzle insert in orange, the confined test section, and the downstream variable diffuser (slightly closed).

Figure 3: Experimental wind-tunnel configuration used for the HTLES validation case. The facility view identifies the physical measurement setup, whereas the CAD view highlights the geometric components reproduced in the numerical model.

the validation case and common comparison quantities, then describe the experimental operation and measurement approach, before presenting the corresponding numerical HTLES setup.

2.1 Validation Case

The validation is *not* based on testing a dedicated model inside a wind tunnel. Instead, the entire wind-tunnel configuration becomes the testbed itself, including a custom nozzle insert modelled after the aft section of a generic planar ETT pod, Fig. 4. The same full wind-tunnel geometry was 3D scanned, then manually postprocessed and optimised in CAD for use in CFD, allowing a direct comparison between experiment and simulation.

2.1.1 Geometry

Experiments are conducted at the FH Aachen intermittent trans- and supersonic indraft wind tunnel. The wind tunnel has a rectangular cross-section of 100 mm by 100 mm in the test section. The upper wall is planar and aligned with the streamwise direction, whereas the lower wall is defined by an interchangeable nozzle insert. The contour of this insert sets the local area distribution and therefore significantly influences the operating condition and Mach number in the test section. The minimum throat cross-section has a height of 40 mm and a spanwise depth of 100 mm. In the present configuration, the planar aft-pod contour is defined as a quarter ellipse with semi-major axis $a = 37.5$ mm and semi-minor axis $b = 15$ mm, giving an aspect ratio of $a/b = 2.5$. This ratio is consistent with generic aft-body shapes used in previous ETT aerodynamic studies [3, 10] and provides a reduced but experimentally accessible representation of the confined SWBLI problem considered in the previous numerical-only study. Access for optical measurements is provided through circular side windows, which are used for the differential-

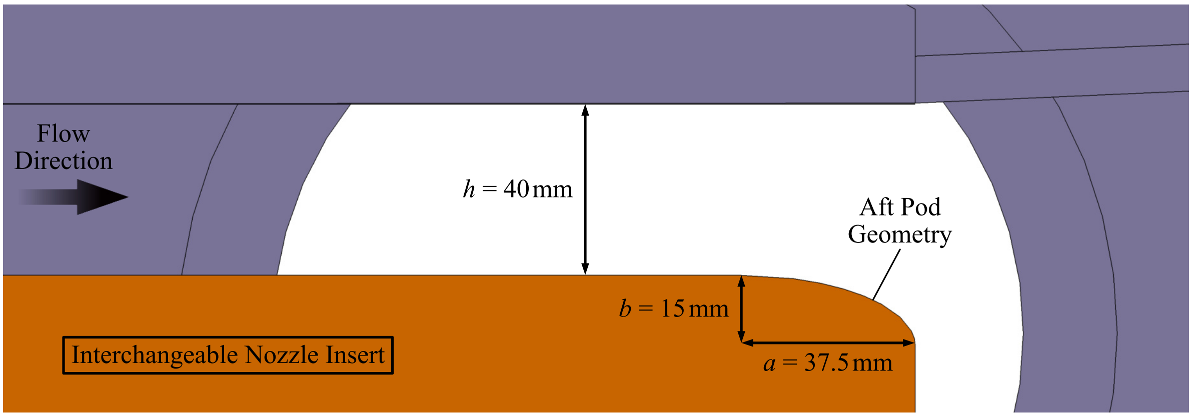

Figure 4: Geometry of the nozzle insert with the simplified aft section of the ETT pod. The model depth is $t = 100$ mm in the wind-tunnel setup and $t = 50$ mm in the numerical setup.

interferometry measurements. Downstream of the test section, a variable diffuser with the same nominal depth as the test section, 100 mm, is used to control the back pressure. The diffuser opening can be varied between 0 mm to 110 mm, allowing the desired operating points to be set reproducibly for the validation experiments. The variable diffuser is therefore treated as part of the shared validation geometry, rather than only as an experimental operating device.

2.1.2 Operating Points and Validation Strategy

The present work focuses on the early part of Regime (II), where the flow state has passed the isentropic limit but has not yet developed into a more stable shock-train configuration. Two operating points are selected within this regime. The first operating point, OP1, set by a 44 mm diffuser opening, represents intermittent transonic shock buffet, where a near-normal shock appears near the aft end of the pod-like insert, travels upstream, breaks down, and reappears further downstream (Cat. (A)). The second operating point, OP2, set by a 46 mm diffuser opening, represents an oscillating λ-shock configuration, where the shock remains present but still oscillates about a mean position (Cat. (B)). They are therefore selected as the validation targets, because they contain the spectrally relevant shock-motion behaviour for which the previous numerical study showed the clearest differences between URANS and HTLES. The intermittent OP1 case is analysed in full, including the image-based shock-motion spectra, whereas OP2 serves as an additional validation point focused on the shock topology. We base our operating-point definition and validation work on two key measurements.

1) A pre-shock Mach number is derived from wall static-pressure measurements and provides a mean operating-point proxy for matching the experimental and numerical conditions.
2) High-speed quasi-schlieren image sequences are obtained with an infinite-fringe differential-interferometry setup and are used to assess the overall shock topology and extract the spectral content of the shock motion.

Details on wind-tunnel operations and the optical measurement setup are further described in Sec. 2.2.

2.2 Experimental Methodology

This subsection provides details on the operational parameters in the experimental wind-tunnel work and the data and image acquisition used for the validation measurements.

2.2.1 Wind-Tunnel Operation

The indraft tunnel is driven by a 24 m^3 vacuum tank and an atmospheric-pressure reservoir of dehumidified air with matching volume. The working-section assembly, consisting of nozzle, windowed test section, and diffuser, is 1.6 m long, of which 600 mm corresponds to the nozzle section. As discussed in Sec. 2.1, the present configuration uses the custom lower insert defined in Fig. 4. The numerical boundary conditions are matched to the measured reservoir state during the experiments, with $p_{0,\mathrm{res}} \approx 1\,020\,\mathrm{mbar}$ and $T_{0,\mathrm{res}} \approx 25\,^{\circ}\mathrm{C}$. Because the facility is supplied with dehumidified air, the gas properties are modelled using the standard dry-air values $R = 287.1\,\mathrm{J\,kg^{-1}\,K^{-1}}$ and $\gamma = 1.4$, with Sutherland's law used for the dynamic viscosity. Under these conditions, the facility produces a unit Reynolds number on the order of $10 \cdot 10^6\,\mathrm{m^{-1}}$, placing the validation case in a high-Reynolds-number transonic regime relevant to the intended SWBLI comparison. Core-flow turbulence levels were characterised separately in a conventional transonic-nozzle configuration, rather than in the present insert configuration, and were found to be in the range of 2 % to 3 %.

The Mach number upstream of the shock is a key parameter for assessing the operating condition and is determined from the wall static-pressure measurement and the reservoir pressure. The corresponding pressure tap is located 90 mm upstream of the aft-pod end. The pressure-derived pre-shock Mach proxy is then computed as

$$M_{\mathrm{pre}} = \left[\frac{2}{\gamma - 1} \left(\left(\frac{p_{0,\mathrm{res}}}{p_{w,\mathrm{pre}}} \right)^{(\gamma-1)/\gamma} - 1 \right) \right]^{1/2}, \tag{2}$$

where $p_{0,\mathrm{res}}$ is the reservoir pressure used as total-pressure reference and $p_{w,\mathrm{pre}}$ is the wall static pressure upstream of the shock. The resulting value is treated as an operating-point proxy because it is based on wall-pressure data and an isentropic pre-shock estimate rather than a full-field Mach number measurement. Because the tap lies upstream of the sonic region, the proxy remains subsonic and does not represent the local Mach number immediately ahead of the shock. The same pressure-based operating-point definition is reproduced in the CFD setup. There, M_{pre} is monitored with a point probe at the same streamwise position, located outside the boundary layer. A cross-check against a virtual wall-pressure tap evaluated via Eq. (2) showed negligible differences. The wall-pressure data are sampled at 1 kHz. However, the pressure-tubing length further reduces the effective dynamic response. Hence, the pressure signal is used only as a mean-pressure source and not for spectral analysis. Within the analysis window, the Mach proxy is statistically well converged. The RMS fluctuation of the instantaneous proxy remains below $1 \cdot 10^{-3}$ for both operating points, and the type-A uncertainty of the mean stays below $2 \cdot 10^{-4}$ when the autocorrelation of the samples is accounted for. The measurement uncertainty is therefore dominated by the systematic sensor accuracy of just below 5 mbar, which propagates to a Mach-proxy uncertainty of at most ±0.009. Even this bound remains below the experiment-to-simulation differences discussed in Sec. 3.

The unsteady shock dynamics themselves are evaluated primarily from the image sequences described in the following sections. As the wind tunnel operates in an intermittent indraft mode, the vacuum-chamber pressure downstream of the test section varies during a run. Before each run, the vacuum tank is evacuated to approximately 100 mbar to improve run-to-run repeatability. The nominal run time is then set to 4 s by an automated ball valve, of which approximately 3 s provide quasi-stationary operating conditions. The downstream diffuser is used to control the back pressure acting on the aft end of the pod-like insert, ensuring controlled and repeatable operating conditions. For each operating point, a 0.1 s analysis window is selected from this quasi-stationary part of the run, where the pressure-derived Mach proxy varies slowly and the optical measurements indicate that the shock topology remains in the target regime. The window length matches the numerical sampling window and covers many cycles of the expected shock motion in the 500 Hz to 1 000 Hz range.

2.2.2 Differential Interferometry and Image Acquisition

The side windows of the test section provide optical access for flow visualisation of the aft pod-like insert. Here, we employ an infinite-fringe differential-interferometry setup with a monochrome Photron Mini UX100-M high-speed camera operating at 10 kHz and an exposure time of 50 µs. This acquisition rate resolves the expected shock-motion frequencies by roughly an order of magnitude, while higher rates would reduce the optical resolution. A schematic of the optical arrangement is shown in Fig. 5.

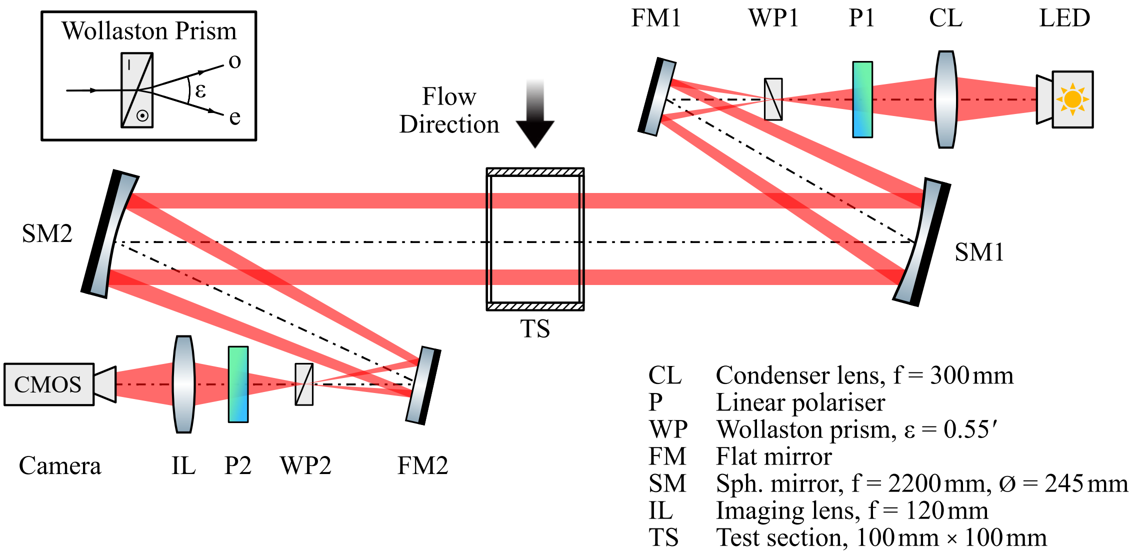

Figure 5: Differential-interferometry flow-visualisation setup with a full-spectrum white LED light source. With both Wollaston prisms placed at their respective focal points, the ordinary (o) and extraordinary (e) beams are sheared by the angle ε, producing an infinite-fringe, schlieren-like image.

In infinite-fringe mode, obtained by placing both Wollaston prisms at the focal points of their spherical mirrors, the arrangement converts refractive-index gradients into intensity variations, producing a quasi-schlieren visualisation whose shear orientation determines the equivalent knife-edge direction [25]. For all measurements reported here, a horizontal equivalent knife-edge direction is used, making the vertical density-gradient component particularly visible. This orientation was selected because it provides clear contrast for the density gradients associated with the boundary layer and SIBLS. The optical shear is set by a quartz Wollaston prism with a nominal full splitting angle of 0.55′. With each Wollaston prism placed in the focal plane of its spherical mirror, the resulting beam separation follows $e = f \tan\varepsilon \approx f\varepsilon$ for small angles, where f is the focal length of the spherical mirrors [26]. For $\varepsilon = 0.55' \approx 1.60 \cdot 10^{-4}$ rad and $f = 2\,200$ mm, this gives $e \approx 0.35$ mm. The camera images are recorded at $1\,280 \times 480$ pixels.

2.2.3 Image Processing and Spectral Data

The high-speed image sequence is processed in two complementary ways. First, the instantaneous quasi-schlieren field is compared with numerical schlieren fields from the HTLES simulations to assess the shock structure and the separated-flow signature. Second, a shock-position time series is extracted by automatically tracking the streamwise location of the dominant shock-related intensity-gradient feature within a fixed region of interest (ROI). The automated tracking procedure is implemented in in-house Python code and validated by tracking three complete shock-buffet cycles by hand, as well as by visual inspection of the complete re-rendered image sequence with the detected shock position overlaid on each frame. This displacement signal is then used to obtain image-based shock-motion spectra for direct comparison with the corresponding numerical spectra. Because each experimental frame is recorded with a finite 50 µs exposure at a 10 kHz acquisition rate, individual frames represent short-time-averaged flow visualisations. This temporal averaging is considered when comparing individual experimental images with instantaneous numerical schlieren fields. For the numerical results, the shock position is tracked with an equivalent criterion based on the strongest density gradient, evaluated directly in the simulation. The experimental and numerical spectra are therefore based on equivalent, though not identical, shock-position observables. Since both criteria track the same dominant shock front, this difference primarily affects the amplitudes rather than the frequency content focused on here.

2.3 Numerical Methodology

The numerical setup, including the computational case definition and the solver configuration, closely follows the authors' previous paper on HTLES in SWBLI flows [3]. The aim of the numerical methodology is to reproduce the same validation case, generate instantaneous numerical schlieren fields from the HTLES solution, and apply the same image- and data-based comparison quantities used for the experiment.

2.3.1 Computational Domain and Boundary Conditions

The geometric setup and computational domain used in the HTLES simulations are based on a 3D-scanned and CFD-optimised digital model [27] of the complete wind-tunnel facility. Core sections, including the nozzle inlet, test section, and diffuser, are reproduced with minimal geometric simplification, while the extended ductwork between the diffuser and vacuum tank is represented only via its cross-sectional area rather than its exact geometry. The digital model allows the operating and boundary conditions to be matched between experiment and CFD and, most importantly, enables the wind-tunnel flow to be driven by the upstream ambient-pressure reservoir and the downstream vacuum tank.

Boundary Conditions The numerical model reproduces the wind-tunnel geometry using a half-domain symmetry approximation. The physical test section has a cross-section of 100 mm × 100 mm, whereas the simulated domain uses a cross-section of 50 mm × 100 mm with a symmetry plane at half the spanwise width. This retains the important cross-sectional area distribution, boundary-layer displacement, nozzle-insert geometry, and downstream diffuser setting while reducing the computational cost. The symmetry plane enforces vanishing instantaneous spanwise velocity and spanwise gradients, which excludes full-width asymmetric and spanwise-travelling modes. The spanwise domain nevertheless remains large relative to the incoming boundary-layer thickness. With an upstream boundary-layer thickness of $\delta \approx 3$ mm to 4 mm, determined optically from the quasi-schlieren images, and $W_{\text{sim}} = 50$ mm, the domain provides $W_{\text{sim}}/\delta > 12$, which is sufficiently wide for the relevant spanwise turbulent structures to develop without directly interacting with the symmetry plane [28, 29]. This argument concerns the resolved turbulent content, whereas the exclusion of asymmetric global shock modes remains a limitation of the half-domain approach. A stagnation inlet is prescribed at the upstream boundary with a total pressure of 1 020 mbar and a total temperature of 25 °C (298.15 K). Inlet turbulence is prescribed in modelled form with an intensity of 2 %, matching the measured core-flow level, and a turbulent viscosity ratio of $\mu_t/\mu = 2$, with the latter chosen following Spalart and Rumsey [30] to counteract the premature decay of modelled turbulence upstream of the test section. Resolved inflow turbulence is not introduced, so the measured core-flow fluctuation level is represented only through the modelled quantities. All solid walls are modelled as stationary adiabatic walls; the adiabatic assumption is justified by the short duration of the experimental runs. At the downstream boundary, a pressure outlet with a constant static pressure of 100 mbar is imposed. This does not reproduce the gradual pressure rise in the vacuum tank, which reaches approximately 200 mbar during the nominal 4 s test time, but the variable diffuser, rather than the tank state, sets the effective back pressure for the test section, making the test-section conditions largely insensitive to the exact tank pressure. In addition, the tank pressure rises by only 2 mbar to 3 mbar during the 0.1 s analysis window.

Initial Conditions All simulations are initialised with the experimental ambient pressure at $t = 0$, before the ball valve opens, throughout the entire domain. A 1 m s^{-1} downstream velocity field is imposed to avoid numerical instability during the first iterations. The flow-through time of the simulated system is on the order of 0.01 s. Each simulation is first advanced for 0.1 s, i.e. approximately ten flow-through times, until a quasi-stationary state is reached. A subsequent 0.1 s window of equal length is then used for statistical sampling and averaging, and all mean values and spectra reported in this paper are evaluated from this window.

2.3.2 Solver Setup and HTLES Model

All simulations are performed in STAR-CCM+ (v2406), where the coupled conservation equations for mass, momentum, and total energy are solved for a viscous compressible ideal gas using an implicit density-based finite-volume formulation. An AUSM+ flux-vector-splitting (FVS) scheme is used for the inviscid fluxes. For the present near-sonic confined flow, this choice was found to slightly reduce the odd–even-type numerical decoupling that can trigger weak Mach-wave patterns particularly visible in the numerical schlieren fields. In the present configuration, this residual wave pattern is likely promoted by the long near-constant-area section[2], over which the flow remains only marginally supersonic and is therefore sensitive to small numerical disturbances. Compared with the Roe scheme used in the authors' previous study [3], this change affects only the inviscid flux discretisation and primarily reduces these numerical wave patterns, and is therefore not expected to affect the comparability of the two studies. Convective fluxes are discretised with the hybrid second-order upwind/bounded-central scheme (hybrid-BCD), combining the stability of second-order upwinding in RANS-dominated or insufficiently resolved regions with the lower numerical dissipation and dispersion of bounded central differencing where scale-resolving behaviour is supported. Time advancement uses an implicit second-order BDF2 scheme with a fixed time step. The mesh-dependent time-step choice and inner-iteration convergence criterion are detailed below.

The turbulent dynamics of the confined transonic flow are treated with Hybrid Temporal Large Eddy Simulation (HTLES), developed by Duffal, de Laage de Meux, and Manceau [4, 5], using the Scale-Resolving Hybrid (SRH) implementation in STAR-CCM+. HTLES is a hybrid RANS–LES method in which the implicit spatial filtering of LES is extended by a temporal filtering step. Each transported quantity can therefore be interpreted as a resolved, filtered part and a subfiltered part,

$$\varphi = \overline{\widetilde{\varphi}} + \varphi' , \tag{3}$$

so that the filtered equations retain a RANS-like transport form while the unresolved contribution is represented by subfiltered-scale stresses. In the eddy-viscosity form used here, these stresses are written as

$$T_{ij}^{\mathrm{SFS}} = 2\mu_t \widetilde{S}_{ij} - \frac{2}{3}\overline{\rho} k_{\mathrm{SFS}} \delta_{ij} , \tag{4}$$

where $\widetilde{S}_{ij}$ is computed from the resolved filtered velocity field, and μ_t and k_{SFS} denote the modelled turbulent viscosity and subfiltered turbulent kinetic energy. The underlying RANS closure is Menter's k–ω SST model, selected because of its established robustness for adverse-pressure-gradient and separated wall-bounded flows [31, 32].

The key HTLES control parameter is the local temporal filter width, which is tied directly to the numerical resolution rather than to prescribed RANS and LES zones. It is defined from the cut-off frequency

$$\Delta T_F(x_i,t) = \frac{2\pi}{\omega_c(x_i,t)}, \qquad \omega_c(x_i,t) = \min\left(\frac{\pi}{\Delta t}, \frac{U_s(x_i,t)\,\pi}{\Delta x(x_i)}\right), \tag{5}$$

where Δt is the physical time step, Δx the local cell size, and U_s the local resolved convective velocity scale. Coarse spatial or temporal resolution increases ΔT_F and drives the equations towards URANS-like behaviour, whereas sufficiently fine local resolution reduces the filter width and allows the large, energy-containing turbulent structures to be resolved in an LES-like manner. This continuous resolution-dependent transition makes HTLES attractive for applied research, because it combines a robust and easy-to-use setup, owing to the reduced pre-processing effort, with scale-resolving results in the resolved regions. In the present study, the near-wall regions and the less resolved regions far upstream and downstream of the test-section area remain modelled, while the shock/separation and wake dynamics can become scale resolving.

[2]The cross-section is only nominally constant, because the growing boundary-layer displacement thickness slowly shifts the effective minimum cross-section downstream.

2.3.3 Computational Mesh and Spatial–Temporal Requirements

The computational mesh is optimised for HTLES as a hybrid RANS–LES approach, where a robust RANS-quality base discretisation is retained for the complete wind-tunnel geometry, while scale-resolving refinement is applied only where the validation physics require it. In the present case, these refinement regions cover the shock-dominated nozzle and test-section region, as well as the separated shear layer and wake downstream of the insert. This strategy keeps the boundary layers and weakly unsteady upstream/downstream duct regions modelled, while providing sufficient local spatial and temporal resolution for the unsteady SIBLS dynamics, covering both the global shock motion and the turbulent structures that may contribute to the feedback mechanism sustaining it.

The finite-volume mesh is generated with a trimmed hexahedral cut-cell/octree approach, giving mostly isotropic cells in the refined core-flow regions. Prism layers are used on all solid walls, and the near-wall treatment follows a low-y^+ RANS strategy, targeting and achieving $y^+ \lesssim 1$ globally. The local refinement level is designed to resolve approximately 80 % of the total turbulent kinetic energy in the LES regions [33, 34]. This design target is translated into a cell-size requirement using preliminary RANS fields to estimate the Taylor-microscale order of magnitude in the critical regions,

$$\lambda = \left(\frac{10\mu}{C_\mu \rho \omega}\right)^{1/2}, \qquad C_\mu = 0.09, \tag{6}$$

which provides a practical $\Delta \sim \lambda$ target for the smallest isotropic cells. In HTLES, this spatial requirement is directly linked to the temporal requirement, because the local cell size and the physical time step together set the cut-off frequency and thus the local transition between RANS-like and LES-like behaviour [35].

Three meshes are used for the present half-domain simulations, containing approximately $4.4 \cdot 10^6$, $11.2 \cdot 10^6$, and $52.3 \cdot 10^6$ cells, with minimal isotropic cell sizes of about 1 mm, 0.5 mm, and 0.25 mm in the shock-separation and wake refinement regions. The physical time step is varied between 50 µs and 2.5 µs across the considered mesh resolutions, Tab. 1, where the smallest time steps approach a convective CFL $= \mathcal{O}(1)$ in the refined regions and the larger steps are included in the temporal sensitivity study. The coupled system is advanced with an AMG V-cycle Gauss–Seidel solver and five non-linear inner iterations per physical time step, selected from preliminary convergence tests to reduce the continuity, momentum, and energy residuals by approximately three orders of magnitude within each step.

2.3.4 Mesh Assessment

For a scale-resolving HTLES setup, mesh adequacy cannot be judged from mean quantities alone, because changing the spatial and temporal resolution also shifts the implicit filter cut-off and therefore the balance between resolved motion and modelled turbulence. We therefore assess the grid independence using two complementary approaches.

a) We evaluate the mean and RMS behaviour of the pre-shock Mach number point-probe monitor[3], which acts as a proxy for shock strength and global unsteadiness, Tab. 1.
b) We examine the resolved spectral content of the axial velocity fluctuation $u'_x = u_x - \overline{u}_x$ within the separated shear layer, Fig. 6.

The meshes show the expected sensitivity to both spatial and temporal resolution. The coarse $4.4 \cdot 10^6$-cell mesh remains a borderline scale-resolving setup. In terms of the mean pre-shock Mach number, the coarse mesh remains offset from the medium and fine meshes by roughly 2 % for time steps of 10 µs and below, indicating that this offset is driven by insufficient spatial resolution. The 50 µs coarse case is additionally affected by temporal filtering, with an RMS level of $1.1 \cdot 10^{-2}$, clearly lower than the $(2.4 - 2.8) \cdot 10^{-2}$ range obtained on the medium and fine meshes, indicating filter-based damping of part of the spectral content. For 10 µs and smaller time steps, the coarse mesh recovers substantially more unsteady content,

[3]The point probe is located 90 mm upstream of the aft section, aligned with the experimental wall-pressure tap.

Table 1: Mesh and time-step resolution study for the half-domain simulations based on the pre-shock Mach number point-probe M_{pre}. The relative difference of $\overline{M}_{\text{pre}}$ is evaluated with respect to the fine-mesh 5.0 µs case and computed from unrounded monitor data.

Mesh	# Cells	$\Delta_{\min}$	Δt	$\overline{M}_{\text{pre}}$	$\Delta\overline{M}_{\text{pre}}$ [%]	$\left(M'_{\text{pre}}\right)_{\text{rms}}$
Coarse	$4.4 \cdot 10^6$	1.0 mm	50 µs	0.934	+1.7	$1.1 \cdot 10^{-2}$
			10 µs	0.906	-1.4	$3.3 \cdot 10^{-2}$
			5.0 µs	0.897	-2.4	$3.4 \cdot 10^{-2}$
			2.5 µs	0.896	-2.4	$3.6 \cdot 10^{-2}$
Medium	$11.2 \cdot 10^6$	0.5 mm	5.0 µs	0.918	0.0	$2.4 \cdot 10^{-2}$
			2.5 µs	0.922	+0.4	$2.6 \cdot 10^{-2}$
Fine	$52.3 \cdot 10^6$	0.25 mm	5.0 µs	0.918	–	$2.7 \cdot 10^{-2}$
			2.5 µs	0.919	+0.1	$2.8 \cdot 10^{-2}$

with $(M'_{\text{pre}})_{\text{rms}}$ increasing to $(3.3-3.6) \cdot 10^{-2}$. This is consistent with the authors' previous observation that HTLES can improve spectral response over URANS even on meshes coarser than normally preferred for hybrid RANS–LES applications [3].

A clear change occurs between the coarse and medium meshes. On the medium $11.2 \cdot 10^6$-cell mesh, $\overline{M}_{\text{pre}} = 0.918$ for $\Delta t = 5.0$ µs, matching the fine-mesh reference case, and halving the time step changes the mean value marginally by only 0.4 %. The fine $52.3 \cdot 10^6$-cell mesh shows an even smaller time-step sensitivity, with $\overline{M}_{\text{pre}}$ changing from 0.918 to 0.919, corresponding to only 0.1 %. The RMS values for the medium and fine cases remain within the narrow range $(2.4-2.8) \cdot 10^{-2}$, indicating that the resolved shock-system fluctuations are no longer primarily controlled by the mesh and time-step choice beyond the medium resolution.

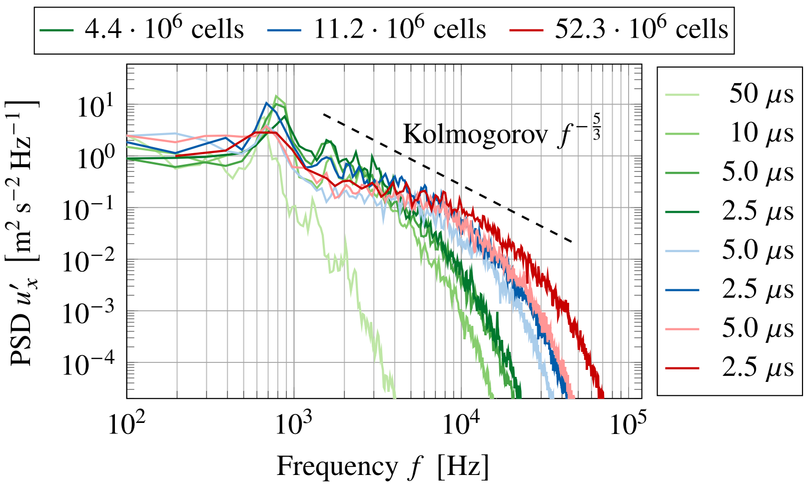

Figure 6: Power spectral density of u'_x at a point probe in the near separated wake. Colours denote the mesh resolution, while different shades of the same colour indicate the temporal resolution. The reference line indicates Kolmogorov's $-5/3$ scaling law (K41).

To check that this behaviour is not limited to the monitored shock-strength proxy M_{pre}, Fig. 6 compares the power spectral density (PSD) of u'_x at a point probe in the separated wake, computed with Welch's method using $n_{\text{perseg}} = 1024$ except for the 50 µs case, where the segment length was reduced because of the lower sampling rate. The spectral distributions show an inertial-like range close to the Kolmogorov $f^{-5/3}$ reference, followed by a steeper decline towards the dissipative regime. The indicated cut-off frequencies, marking the onset of the dissipative Kolmogorov regime, should not be interpreted as purely physical dissipation limits, because coarser meshes and lower sampling rates introduce implicit LES filtering in both space and time. This is visible as an extension of the resolved bandwidth with increasing mesh and time-step resolution. The absolute spectral limit remains the Nyquist frequency $f_\mathrm{N} = f_s/2$, e.g. $f_\mathrm{N} = 50\,\mathrm{kHz}$ for $\Delta t = 10\,\mu\mathrm{s}$ and $f_\mathrm{N} = 200\,\mathrm{kHz}$ for $\Delta t = 2.5\,\mu\mathrm{s}$. The medium and fine configurations preserve the low-frequency content relevant to shock motion, while the main differences appear at the high-frequency end of the spectrum. A further time-step reduction on the fine $52.3 \cdot 10^6$-cell mesh would likely reduce numerical filtering further, but was not computationally feasible within the applied scope of this study.

All HTLES results presented in Sec. 3 are obtained from the fine-mesh configuration with $52.3 \cdot 10^6$ cells and $\Delta t = 5.0\,\mu\mathrm{s}$. Based on the presented assessment, the medium mesh with time steps between $5.0\,\mu\mathrm{s}$ and $2.5\,\mu\mathrm{s}$ captures the relevant shock and turbulence dynamics at substantially lower cost and would be the preferred configuration for broader parameter studies.

3. Results and Discussion

This section covers the experimental validation of the HTLES results in three steps. First, the two selected operating points are placed into the expected shock-motion regimes using the visual flow state, and the non-dimensional frequency scaling is introduced. Second, the intermittent shock-buffet case at the 44 mm diffuser setting is analysed in detail, because it represents the most demanding validation target. Third, the 46 mm diffuser setting is used as an additional validation point, where the shock topology is more stable but still contains the relevant oscillating λ-shock behaviour. The section concludes with instantaneous HTLES visualisations that combine numerical schlieren images with Q-criterion isosurfaces of the resolved flow.

3.1 Operating-Regime Classification and Frequency Scaling

The two operating points selected in Sec. 2.1 represent two flow states just above the isentropic limit. The 44 mm case is representative of a Cat. (A) flow, i.e. intermittent transonic shock buffet. In this configuration, the shock does not remain at a fixed mean location for a complete buffet cycle, but repeatedly appears near the aft part of the insert, travels upstream, breaks down, and reappears further downstream. The 46 mm case is representative of Cat. (B) flow, where a λ-shock is permanently present and oscillates around a mean position. This distinction is important, because both cases are located in the same general near-isentropic-limit regime, but they represent different degrees of global shock-system stability.

For the spectral comparison, the experimental data were extracted automatically from the high-speed quasi-schlieren image series using the procedure described in Sec. 2.2. Within a fixed ROI, the in-house code first normalises the local background to reduce sensitivity to slow illumination drift, then evaluates the streamwise intensity gradient of the monochrome image data with a Scharr operator, projects its magnitude across the ROI height, and tracks the dominant peak frame by frame as the streamwise shock position. For the numerical CFD data, a custom field function tracks the shock position based on the strongest density gradient on the nozzle-insert surface, evaluated along the symmetry plane so that the detected position cannot jump in the spanwise direction. Since we do not compare the absolute time-series data, but focus on the frequency domain, all position signals are expressed in arbitrary units and the resulting spectra are normalised.

To relate the observed shock motion to other buffet-like transonic flows, the dominant frequencies are also expressed in non-dimensional form using the Strouhal number,

$$St = \frac{f\,L_\mathrm{ref}}{U_\mathrm{ref}}\,, \tag{7}$$

where f denotes the shock-motion frequency. For the present wind-tunnel configuration, $U_{\mathrm{ref}} = 316\,\mathrm{m\,s^{-1}}$ is used, corresponding to the critical speed of sound a^* for the experimental total temperature of approximately 25 °C (298.15 K). The choice of L_{ref} is less direct, because the present confined transonic configuration does not correspond exactly to the canonical cases commonly used in the literature. Classical transonic wing buffet is usually normalised with the chord length, whereas impinging-shock SWBLI configurations often use an interaction length associated with the separated region. Neither definition is directly applicable here. Possible reference lengths range from the semi-minor axis of the elliptical rear geometry, 15 mm, up to the wind-tunnel height of 40 mm. We adopt the semi-major axis of the pod rear geometry, $L_{\mathrm{ref}} = 37.5\,\mathrm{mm}$, as the representative value, because it is the closest analogue to a chord-like length scale, while any choice within the 15 mm to 40 mm range would lead to the same order of magnitude when comparing with literature Strouhal numbers. According to the literature, two-dimensional transonic turbulent shock buffet typically occurs at chord-based Strouhal numbers of approximately $St_c = 0.05$ to 0.10 [36].

3.2 Cat. (A): Intermittent Shock Buffet

The first validation case is the 44 mm diffuser setting. This case is used as the main comparison because it contains the complete intermittent shock-buffet cycle and is considered more critical due to its intermittent nature. Table 2 summarises the quantitative comparison for both operating points.

For the qualitative comparison, we sample image series from the numerical and experimental results, each representing a single intermittent buffet cycle, Fig. 7. In the experimental sequence, one complete cycle spans roughly 15 frames at the 10 kHz acquisition rate, corresponding to a cycle duration of approximately 1.5 ms. In the quasi-schlieren images, the horizontal equivalent knife-edge direction emphasises the boundary layer and the separated shear wake, but reduces the contrast of the near-vertical shock fronts. This orientation also allows an optical estimate of the incoming boundary-layer thickness, which slightly overpredicts the conventional δ_{99} value and therefore serves as an upper bound. Experiment and simulation both show $\delta \approx 3\,\mathrm{mm}$ to 4 mm upstream of the interaction. The images are shown without contrast or colour adjustment to preserve the recorded intensity information, so the shock fronts and the separated shear layer appear at low contrast but remain identifiable.

Table 2: Quantitative validation summary for both operating points. The pre-shock Mach proxy $\overline{M}_{\mathrm{pre}}$ follows Eq. (2), evaluated 90 mm upstream of the aft-pod end and averaged over the 0.1 s analysis window. Relative differences are computed from unrounded data. The Strouhal number uses the chord-like reference length $L_{\mathrm{ref}} = 37.5\,\mathrm{mm}$ with $U_{\mathrm{ref}} = a^* = 316\,\mathrm{m\,s^{-1}}$ (Sec. 3.1).

			Exp.	HTLES	Δ [%]
OP1 (Cat. (A))	$\overline{M}_{\mathrm{pre}}$	[–]	0.898	0.918	+2.3
	f_{peak}	[Hz]	680	680	$< 1.5^{a}$
	St	[–]	0.08	0.08	–
OP2 (Cat. (B))	$\overline{M}_{\mathrm{pre}}$	[–]	0.917	0.934	+1.9

[a] Experimental and numerical peaks fall within the same frequency bin; the resolvable difference is limited by the 0.1 s analysis window ($\Delta f = 10\,\mathrm{Hz}$).

The comparison in Fig. 7 highlights the key qualitative validation result. Both data sets show the same four-state sequence, presented row by row in Fig. 7, with 1) shock formation near the aft end of the insert, 2) upstream motion of the primary shock into the throat region, 3) shock breakdown once the conditions for a shock are no longer met, and 4) downstream reappearance of the shock system, restarting the cycle. This is the same physical sequence that was observed in the previous numerical-only study, now recovered in the experiment. Since the experimental run and the simulation are not phase locked, the images are compared at equivalent phases of the cycle rather than at identical absolute times. On this basis, the

(a) HTLES, downstream appearance

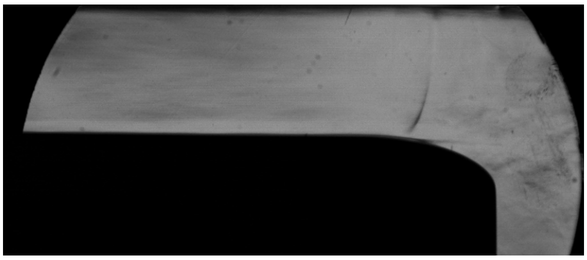

(b) Experiment, downstream appearance

(c) HTLES, upstream motion

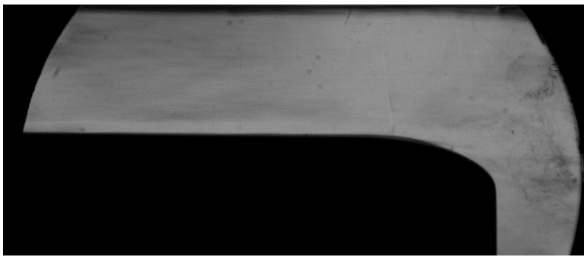

(d) Experiment, upstream motion

(e) HTLES, shock breakdown

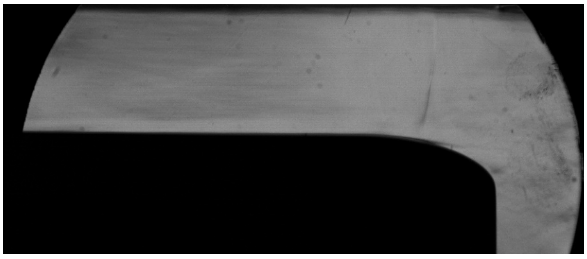

(f) Experiment, shock breakdown

(g) HTLES, downstream reappearance

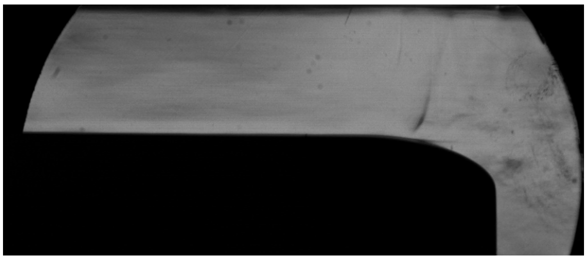

(h) Experiment, downstream reappearance

Figure 7: Image-sequence comparison of the intermittent transonic shock-buffet cycle for the 44 mm diffuser setting. HTLES numerical schlieren images on the left, experimental quasi-schlieren images on the right.

comparison demonstrates that HTLES reproduces the same sequence of distinct flow states, including the separated region downstream of the shock foot and the intermittent loss of a coherent shock structure.

For a more quantitative comparison, we analyse the shock-position signals in the frequency domain using a discrete Fourier transform (DFT), Fig. 8. The spectra are normalised by their respective maximum amplitude, because the numerical signal is derived directly from a shock-position measure in the simulation, whereas the experimental signal is extracted from image data and therefore affected by optical shear, exposure time, illumination, and camera response. The expected validation outcome is a match of the dominant frequency band and major spectral peaks, not an exact equality of amplitudes.

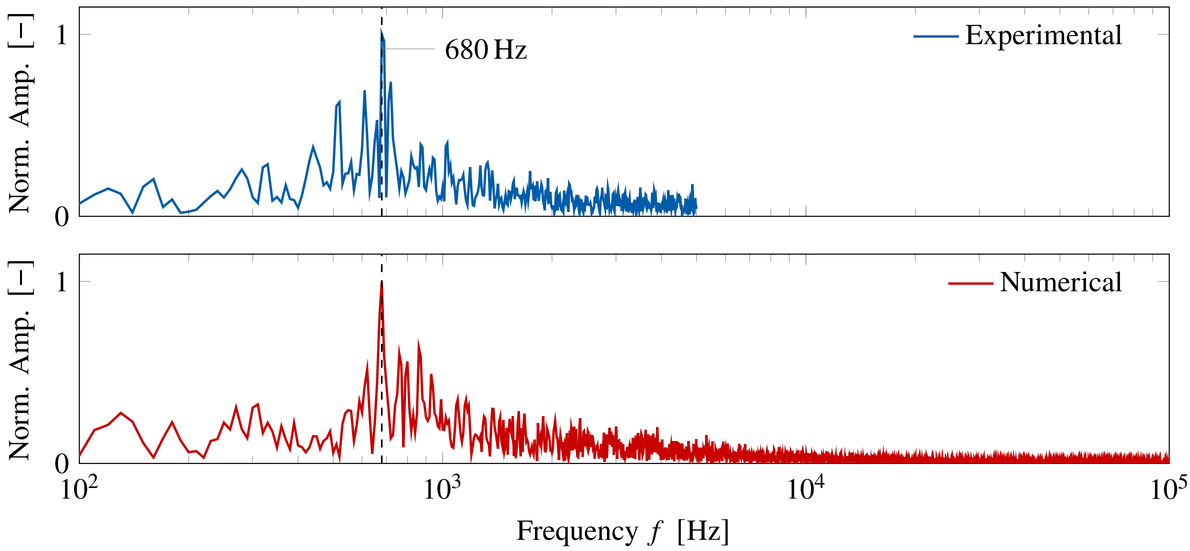

Figure 8: Spectral response of the shock-wave position for the 44 mm case. The amplitudes are normalised to compare the dominant frequency bands and peak locations. The experimental bandwidth is limited by the 10 kHz acquisition rate, whereas the numerical spectrum extends further due to its smaller sampling interval.

The spectral comparison provides the main validation argument for the unsteady part of the flow field. Since even steady RANS models predict the mean shock position reasonably well for this type of configuration [3], the focus here is on confirming that the spectral response predicted by HTLES, which URANS did not recover in the authors' previous study, is a physical effect. Figure 8 shows overall similar spectral behaviour between experiment and simulation and, most importantly, a distinct overlap of the dominant peak at 680 Hz. With both signals sampled over 0.1 s, the DFT resolution is limited to $\Delta f = 1/T = 10$ Hz, so the matching peaks indicate that both fall within the same 10 Hz frequency bin around 680 Hz. The analysis window covers roughly 70 cycles of this dominant motion. Within this resolution, the simulation recovers the global shock-motion timescale of the experiment, consistent with the cycle duration observed directly in the image sequence. The wake PSD of Fig. 6 provides an additional, independent indicator of this timescale. The velocity spectra contain a distinct peak in the 650 Hz to 800 Hz band, which the medium and, at lower amplitude, the fine mesh place near 680 Hz, whereas the coarse mesh shifts it towards 800 Hz. Since the point probe is located downstream in the separated wake, this peak is only a proxy for the shock motion. It confirms, however, that the global shock-system unsteadiness imposes itself on the resolved wake dynamics. Expressed in the non-dimensional form of Eq. (7) with the chord-like reference length $L_{\text{ref}} = 37.5$ mm, the peak frequency corresponds to $St \approx 0.08$, which lies within the $St_c = 0.05$ to 0.10 band reported for two-dimensional transonic shock buffet [36]. At matched Mach number and Strouhal scaling, the same shock motion on a full-scale pod with a reference length on the order of 1 m corresponds to frequencies on the order of 25 Hz, placing the observed dynamics in the 10 Hz to 100 Hz band most relevant for structural excitation and passenger comfort. This is the relevant improvement over steady or weakly unsteady RANS-type approaches, because the validation target is not only the presence of a shock or the mean separated-flow structure, but the spectral behaviour of the shock-induced separation itself.

3.3 Cat. (B): Oscillating λ-Shock

The second validation case is the 46 mm diffuser setting, where the shock system remains present over the complete analysed sequence. We therefore do not repeat the full image-sequence comparison. Instead, Fig. 9 compares one representative instantaneous numerical schlieren field with one experimental quasi-schlieren frame. This comparison focuses on the shock topology, particularly on whether both data sources show the same λ-shock structure and the same qualitative separated-flow signature downstream of the shock foot.

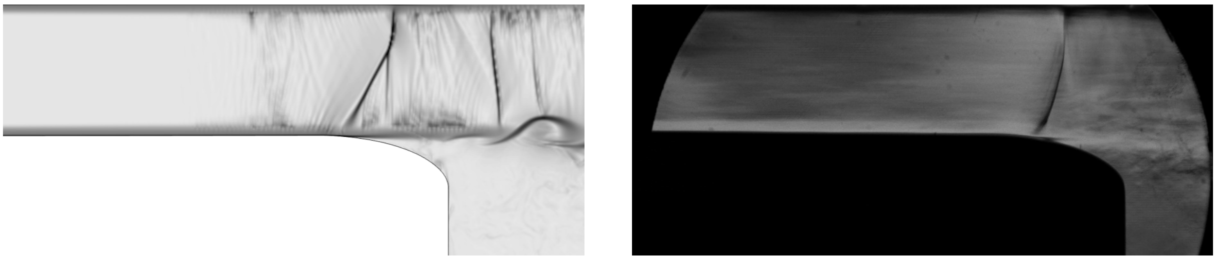

(a) HTLES numerical schlieren

(b) Experimental quasi-schlieren

Figure 9: Shock-topology comparison for the 46 mm diffuser setting. The operating point represents Cat. (B), where an established λ-shock remains present but oscillates about a mean position.

The observed topology in Fig. 9 is consistent with the expected development from intermittent shock buffet towards a more established shock system. The main shock remains attached to a separated boundary-layer region and does not undergo the breakdown observed in the intermittent case. This does not imply a steady flow field. Instead, the flow has moved from a collapse/reformation cycle into an oscillatory λ-shock state. From a validation perspective this is useful, because it tests whether HTLES also reproduces the less intermittent part of the same operating-regime family.

The operating-point comparison in Tab. 2 supports this topology-based assessment. The pressure-derived pre-shock Mach proxy agrees within 1.9 % for the 46 mm case and within 2.3 % for the intermittent 44 mm case, with HTLES slightly overpredicting the experimental value at both operating points. The similar magnitude and sign of this deviation indicate a systematic origin rather than a case-dependent mismatch. It is noted that the coarse-mesh cases in Tab. 1 happen to lie closer to the experimental value. This agreement is regarded as a coincidental cancellation of resolution and modelling errors, and the grid-converged solution with its small systematic offset remains the meaningful comparison. An image-based spectral evaluation of the oscillating λ-shock motion, analogous to Fig. 8, is beyond the scope of this initial validation study and is the designated next step for this operating point. Together, the two operating points cover the transition from Cat. (A) to Cat. (B), which is the part of the regime map most relevant to shock-induced unsteady loading in the present confined transonic configuration.

3.4 Instantaneous Resolved Flow Structures

Finally, Fig. 10 shows instantaneous numerical schlieren images combined with Q-criterion isosurfaces coloured by the local Mach number for the Cat. (A) and Cat. (B) cases. This figure is not used as an additional experimental validation metric, but it highlights two aspects of the resolved flow. First, the strong turbulence production at the shock foot underlines the shock-induced nature of the separation. Second, the separated flow and its coherent turbulent structures show a clear upward tendency. This behaviour differs distinctly from the authors' previous numerical-only configuration and may indicate the influence of the mismatched outer-wall boundary conditions, i.e. the stationary upper wall of the wind tunnel as opposed to the moving tube wall representative of an actual ETT system.

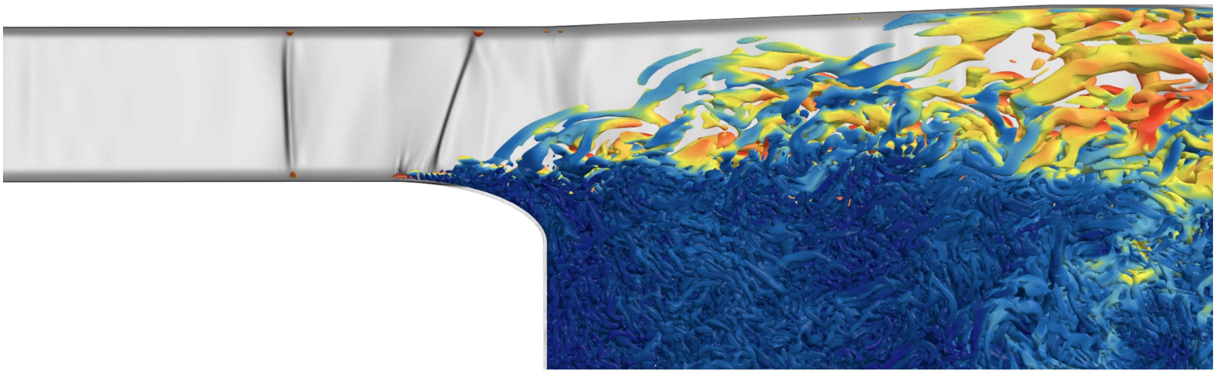

(a) Instantaneous resolved shock/separation topology for Cat. (A) flow conditions

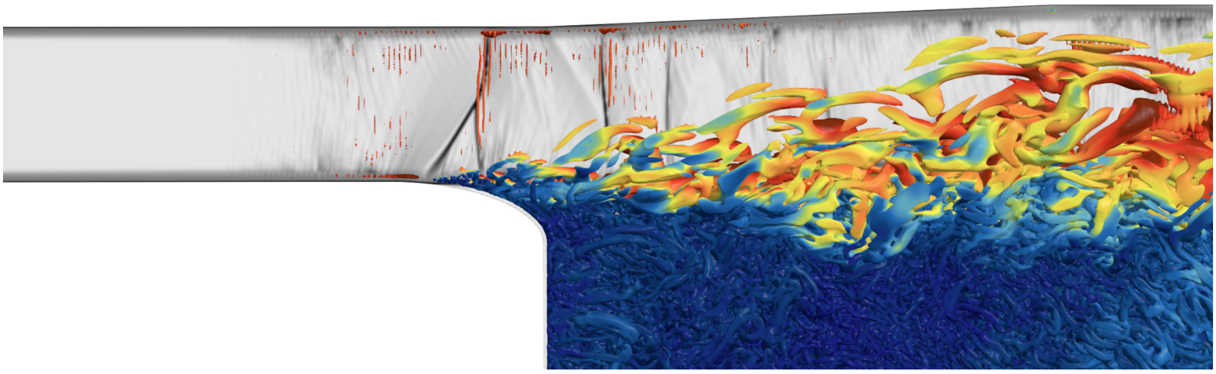

(b) Instantaneous resolved shock/separation topology for Cat. (B) flow conditions

Figure 10: Instantaneous HTLES visualisations of the shock-induced separation and the resolved flow structures. The numerical schlieren field is combined with Q-criterion isosurfaces coloured by Mach number to show the relation between the shock system, the separated shear layer, and the downstream wake.

In addition, Fig. 10b shows secondary density-gradient structures downstream of the λ-shock. These structures were also clearly visible in the previous numerical work and appear to lie on the border between weak shock waves and acoustic Mach waves. They travel upstream and may reinforce the coupling mechanism between the separated wake and the transonic buffet-like shock motion. In contrast to the weak stationary wave patterns of numerical origin discussed in Sec. 2.3, these structures are unsteady and propagate upstream, which points to a physical acoustic mechanism rather than a numerical artefact. Their direct confirmation in the experimental image sequences is left for future evaluation. Resolving such features further supports the use of scale-resolving simulations to physically reproduce the working mechanisms of the present flow.

The instantaneous visualisation therefore supports the interpretation of the spectral results. The shock motion observed in the image-based spectra is not an isolated optical feature, but part of a coupled system of shock motion, separation, and wake dynamics. While URANS can recover transonic shock buffet on airfoils and wings when appropriately configured [2, 37], it did not recover the spectral behaviour of the present blunt-body confined transonic flow in the authors' previous study [3]. Whether this buffet-like shock motion is governed by the same instability mechanism as classical transonic buffet remains an open question. For this class of flows, however, the present validation demonstrates that HTLES captures the coupled shock and separated-flow dynamics reliably and at feasible computational cost, which URANS has so far not achieved.

Regarding computational cost, the fine-mesh 0.1 s sampling run with $\Delta t = 5.0\,\mu\text{s}$ required approximately 96 h on three Nvidia H100 GPUs (96 GB HBM2e each, NVLink-coupled). The same throughput was achieved on four CPU nodes with two Intel Xeon 8468 processors (2.1 GHz, 48 cores) and 256 GB memory each. The medium mesh remained within reach of local workstation hardware. The largest cases were computed on RWTH Aachen CLAIX HPC resources.

4. Conclusion and Outlook

This paper presented a first step towards the experimental validation of HTLES for confined transonic flows dominated by shock-induced boundary-layer separation, as encountered by ETT systems operating near the isentropic limit. The validation is built on a matched configuration in which the complete transonic indraft wind tunnel, equipped with a nozzle insert representing a generic aft pod section, was investigated experimentally and numerically. Two operating points just above the isentropic limit were selected, an intermittent transonic shock-buffet state (Cat. (A)) and an established oscillating λ-shock state (Cat. (B)). The experimental data comprise high-speed infinite-fringe differential-interferometry image sequences and wall static-pressure measurements, which are compared with numerical schlieren fields and shock-position spectra from HTLES simulations of the digitally reconstructed wind tunnel.

For the intermittent case, HTLES reproduces the complete experimentally observed buffet cycle, including shock formation near the aft end of the insert, upstream motion, breakdown, and downstream re-formation. The dominant shock-motion frequency matches the experimental value of 680 Hz within the 10 Hz resolution of the spectral analysis, corresponding to a chord-like Strouhal number of $St \approx 0.08$ and thus to the range reported for two-dimensional turbulent transonic shock buffet. Scaled to full-size pod dimensions, this motion falls into the 10 Hz to 100 Hz band relevant for structural excitation and passenger comfort. The pressure-derived pre-shock Mach proxy agrees within 2.3 % and 1.9 % for the two operating points, with a consistent small overprediction by HTLES. Some deviation is expected this close to the isentropic limit, where the near-sonic flow responds sensitively to small changes in the operating conditions. More importantly, both operating points deviate with the same trend, indicating a systematic origin that did not impair the spectral agreement and the shock-topology match. For the λ-shock case, the simulation recovers the experimentally observed shock topology and separated-flow signature. Together, these results provide experimental support for the authors' previous numerical-only findings and present HTLES as a practical scale-resolving method for unsteady SWBLI in confined transonic transport applications.

Future work will extend the validation to image-based spectra of the oscillating λ-shock case and to full-width simulations without the symmetry approximation, which currently excludes asymmetric shock modes. Whether the blunt-body buffet-like shock motion shares the instability mechanism of classical transonic buffet also remains an open question. With the validated combination of high-speed flow visualisation and HTLES, these questions can now be addressed with confidence, bringing reliable spectral predictions of unsteady SWBLI within reach of early-stage development of confined transonic transport systems.

Acknowledgements

The authors express their gratitude to Siemens Digital Industries Software for providing academic licences for Simcenter STAR-CCM+. Computations were performed with computing resources granted by RWTH Aachen University under project RWTH1693.

References

[1] Holger Babinsky and John Harvey. *Shock wave-boundary-layer interactions*. Cambridge aerospace series. Cambridge University Press, Cambridge and New York, 2011.

[2] Nicholas F. Giannelis, Gareth A. Vio, and Oleg Levinski. A review of recent developments in the understanding of transonic shock buffet. *Progress in Aerospace Sciences*, 92:39–84, July 2017.

[3] Benedikt Geiben, Marc Havermann, Errol Hale, and Cees Bil. Application of hybrid-temporal LES to shock-induced boundary layer separation in hyperloop flows. *CEAS Aeronautical Journal*, November 2025.

[4] Vladimir Duffal, Benoît de Laage Meux, and Rémi Manceau. Development and Validation of a Hybrid RANS-LES Approach Based on Temporal Filtering. In *Volume 2: Computational Fluid Dynamics*. American Society of Mechanical Engineers, 2019.

[5] Vladimir Duffal, Benoît de Laage Meux, and Rémi Manceau. Development and Validation of a New Formulation of Hybrid Temporal Large Eddy Simulation. *Flow, Turbulence and Combustion*, 108(1):1–42, 2022.

[6] Max M. J. Opgenoord and Philip C. Caplan. Aerodynamic Design of the Hyperloop Concept. *AIAA Journal*, 56(11):4261–4270, 2018.

[7] Alex J. Lang, David P. Connolly, Gregory de Boer, Shahrokh Shahpar, Benjamin Hinchliffe, and Carl A. Gilkeson. A review of Hyperloop aerodynamics. *Computers & Fluids*, 273:106202, 2024.

[8] Kyeong Sik Jang, Thi Thanh Giang Le, Jihoon Kim, Kwan-Sup Lee, and Jaiyoung Ryu. Effects of compressible flow phenomena on aerodynamic characteristics in Hyperloop system. *Aerospace Science and Technology*, 117:106970, 2021.

[9] Qiujun Yu, Xiaofeng Yang, Jiqiang Niu, Yang Sui, Yanxia Du, and Yanping Yuan. Theoretical and numerical study of choking mechanism of fluid flow in Hyperloop system. *Aerospace Science and Technology*, 121:107367, 2022.

[10] Maurice Bizzozero, Yohei Sato, and Mohamed Aly Sayed. Aerodynamic study of a Hyperloop pod equipped with compressor to overcome the Kantrowitz limit. *Journal of Wind Engineering and Industrial Aerodynamics*, 218:104784, 2021.

[11] Zhiwei Zhou, Chao Xia, Xuzhi Du, Xizhuang Shan, and Zhigang Yang. Impact of the isentropic and Kantrowitz limits on the aerodynamics of an evacuated tube transportation system. *Physics of Fluids*, 34(6), 2022.

[12] Yang Sui, Jiqiang Niu, Qiujun Yu, Yanping Yuan, Xiaoling Cao, and Xiaofeng Yang. Numerical analysis of the aerothermodynamic behavior of a Hyperloop in choked flow. *Energy*, 237:121427, 2021.

[13] V. I. Zvegintsev, S. O. Morozov, and D. G. Nalivaychenko. Gas dynamics of the uniform body acceleration in the channel. In *AIP Conference Proceedings*, AIP Conference Proceedings, page 030012. Author(s), 2018.

[14] B. H. K. Lee. Oscillatory shock motion caused by transonic shock boundary-layer interaction. *AIAA Journal*, 28(5):942–944, May 1990.

[15] J. D. Crouch, A. Garbaruk, and D. Magidov. Predicting the onset of flow unsteadiness based on global instability. *Journal of Computational Physics*, 224(2):924–940, June 2007.

[16] J. D. Crouch, A. Garbaruk, D. Magidov, and A. Travin. Origin of transonic buffet on aerofoils. *Journal of Fluid Mechanics*, 628:357–369, June 2009.

[17] N. D. Sandham, Y. F. Yao, and A. A. Lawal. Large-eddy simulation of transonic turbulent flow over a bump. *International Journal of Heat and Fluid Flow*, 24(4):584–595, 2003.

[18] Philippe R. Spalart, Kirill V. Belyaev, Andrey V. Garbaruk, Mikhail L. Shur, Mikhail Kh. Strelets, and Andrey K. Travin. Large-Eddy and Direct Numerical Simulations of the Bachalo-Johnson Flow with Shock-Induced Separation. *Flow, Turbulence and Combustion*, 99(3-4):865–885, 2017.

[19] Julien Dandois, Ivan Mary, and Vincent Brion. Large-eddy simulation of laminar transonic buffet. *Journal of Fluid Mechanics*, 850:156–178, 2018.

[20] Jiqiang Niu, Yang Sui, Qiujun Yu, Xiaoling Cao, and Yanping Yuan. Numerical study on the impact of Mach number on the coupling effect of aerodynamic heating and aerodynamic pressure caused by a tube train. *Journal of Wind Engineering and Industrial Aerodynamics*, 190:100–111, 2019.

[21] Sha Zhong, Bosen Qian, Mingzhi Yang, Fan Wu, Tiantian Wang, Changda Tan, and Jiangchuan Ma. Investigation on flow field structure and aerodynamic load in vacuum tube transportation system. *Journal of Wind Engineering and Industrial Aerodynamics*, 215:104681, 2021.

[22] Xiao Hu, Zigang Deng, Jiwang Zhang, and Weihua Zhang. Aerodynamic behaviors in supersonic evacuated tube transportation with different train nose lengths. *International Journal of Heat and Mass Transfer*, 183:122130, 2022.

[23] Jean M. Delery. Experimental investigation of turbulence properties in transonic shock/boundary-layer interactions. *AIAA Journal*, 21(2):180–185, 1983.

[24] Yongcheol Seo, Minki Cho, Dong Hyeon Kim, Taekki Lee, Jaiyoung Ryu, and Changyoung Lee. Experimental analysis of aerodynamic characteristics in the Hyperloop system. *Aerospace Science and Technology*, 137:108265, 2023.

[25] Harald Kleine and Hans Groenig. Visualization of transient flow phenomena by means of color schlieren and shearing interferometry. In John M. Dewey and Roberto G. Racca, editors, *20th International Congress on High Speed Photography and Photonics*, volume 1801, page 400. SPIE, January 1993.

[26] Herbert Oertel. *Optische Strömungsmesstechnik*. Braun-Verlag, 1989.

[27] Werner Kritzinger, Matthias Karner, Georg Traar, Jan Henjes, and Wilfried Sihn. Digital twin in manufacturing: A categorical literature review and classification. *IFAC-PapersOnLine*, 51(11):1016–1022, 2018. 16th IFAC Symposium on Information Control Problems in Manufacturing INCOM 2018.

[28] Alexander J. Smits, Beverley J. McKeon, and Ivan Marusic. High-Reynolds Number Wall Turbulence. *Annual Review of Fluid Mechanics*, 43(1):353–375, 2011.

[29] Sergio Pirozzoli and Matteo Bernardini. Turbulence in supersonic boundary layers at moderate Reynolds number. *Journal of Fluid Mechanics*, 688:120–168, 2011.

[30] Philippe R. Spalart and Christopher L. Rumsey. Effective inflow conditions for turbulence models in aerodynamic calculations. *AIAA Journal*, 45(10):2544–2553, October 2007.

[31] F. R. Menter. Two-equation eddy-viscosity turbulence models for engineering applications. *AIAA Journal*, 32(8):1598–1605, 1994.

[32] F. R. Menter, Martin Kuntz, and Robin Langtry. Ten years of industrial experience with the SST turbulence model. *Turbulence, heat and mass transfer*, 2003(4):625–632, 2003.

[33] Stephen B. Pope. *Turbulent Flows*. Cambridge University Press, August 2000.

[34] Pierre Sagaut. *Large eddy simulation for incompressible flows: An introduction*. Scientific computation. Springer, Berlin and New York, 3rd ed. edition, 2006.

[35] Sal Rodriguez. *Applied Computational Fluid Dynamics and Turbulence Modeling*. Springer International Publishing, Cham, 2019.

[36] B. H. K. Lee. Self-sustained shock oscillations on airfoils at transonic speeds. *Progress in Aerospace Sciences*, 37(2):147–196, February 2001.

[37] Maximilian Ehrle, Andreas Waldmann, Thorsten Lutz, and Ewald Krämer. Simulation of transonic buffet with an automated zonal des approach. *CEAS Aeronautical Journal*, 11(4):1025–1036, September 2020.